The Sensitivity of Convective Initiation to the Lapse Rate of the Active Cloud-Bearing Layer

ADAM L. HOUSTON

Department of Geosciences, University of Nebraska at Lincoln, Lincoln, Nebraska

DEV NIYOGI

Departments of Agronomy and Earth and Atmospheric Sciences, Purdue University, West Lafayette, Indiana

ABSTRACT

Numerical experiments are conducted using an idealized cloud-resolving model to explore the sensitivity of deep convective initiation (DCI) to the lapse rate of the active cloud-bearing layer [ACBL; the atmospheric layer above the level of free convection (LFC)]. Clouds are initiated using a new technique that involves a preexisting airmass boundary initialized such that the (unrealistic) adjustment of the model state variables to the imposed boundary is disassociated from the simulation of convection. Reference state environments used in the experiment suite have identical mixed layer values of convective inhibition, CAPE, and LFC as well as identical profiles of relative humidity and wind. Of the six simulations conducted for the experiment set, only the three environments with the largest ACBL lapse rates support DCI. The simulated deep convection is initiated from elevated sources (parcels in the convective clouds originate near 1300 m) despite the presence of a surface-based boundary. Thermal instability release is found to be more likely in the experiments with larger ACBL lapse rates because the forced ascent at the preexisting boundary is stronger (despite nearly identical boundary depths) and because the parcels' LFCs are lower, irrespective of parcel dilution. In one experiment without deep convection, DCI failure occurs even though thermal instability is released. Results from this experiment along with the results from a heuristic Lagrangian model reveal the existence of two convective regimes dependent on the environmental lapse rate: a supercritical state capable of supporting DCI and a subcritical state that is unlikely to support DCI. Under supercritical conditions the rate of increase in buoyancy due to parcel ascent exceeds the reduction in buoyancy due to dilution. Under subcritical conditions, the rate of increase in buoyancy due to parcel ascent is outpaced by the rate of reduction in buoyancy from dilution. Overall, results demonstrate that the lapse rate of the ACBL is useful in diagnosing and/or predicting DCI.

1. Introduction

The initiation of deep convection requires (at a minimum) conditional instability (a vertical profile of temperature that can yield the release of thermal instability given parcel saturation) and a trigger (the initial upward motion that releases the thermal instability). A localized trigger for deep convective initiation (DCI) would be unnecessary if the atmosphere was absolutely unstable, but this is usually not the case and more often the atmosphere is characterized by a layer of poten-

tially warm air above the surface [quantified as convective inhibition (CIN)] that inhibits the spontaneous release of thermal instability. However, in situations for which atmospheric preconditioning (Johnson and Mapes 2001) has removed CIN, DCI is still not assured since the dilution of individual air parcels ascending toward the level of free convection (LFC) can increase the actual inhibition of each parcel (Ziegler and Rasmussen 1998). This increase in inhibition typically manifests itself as a cooling of cloudy parcels produced when dilution/entrainment reduces parcel moisture, thereby promoting evaporation. Assessing the dilution of individual air parcels requires relaxing parcel theory, which specifically excludes mixing. In doing so, the parcel LFC becomes a time-dependent quantity that increases with increasing parcel dilution (a parcel cooled

Corresponding author address: Dr. Adam L. Houston, Dept. of Geosciences, University of Nebraska at Lincoln, 214 Bessey Hall, Lincoln, NE 68588.
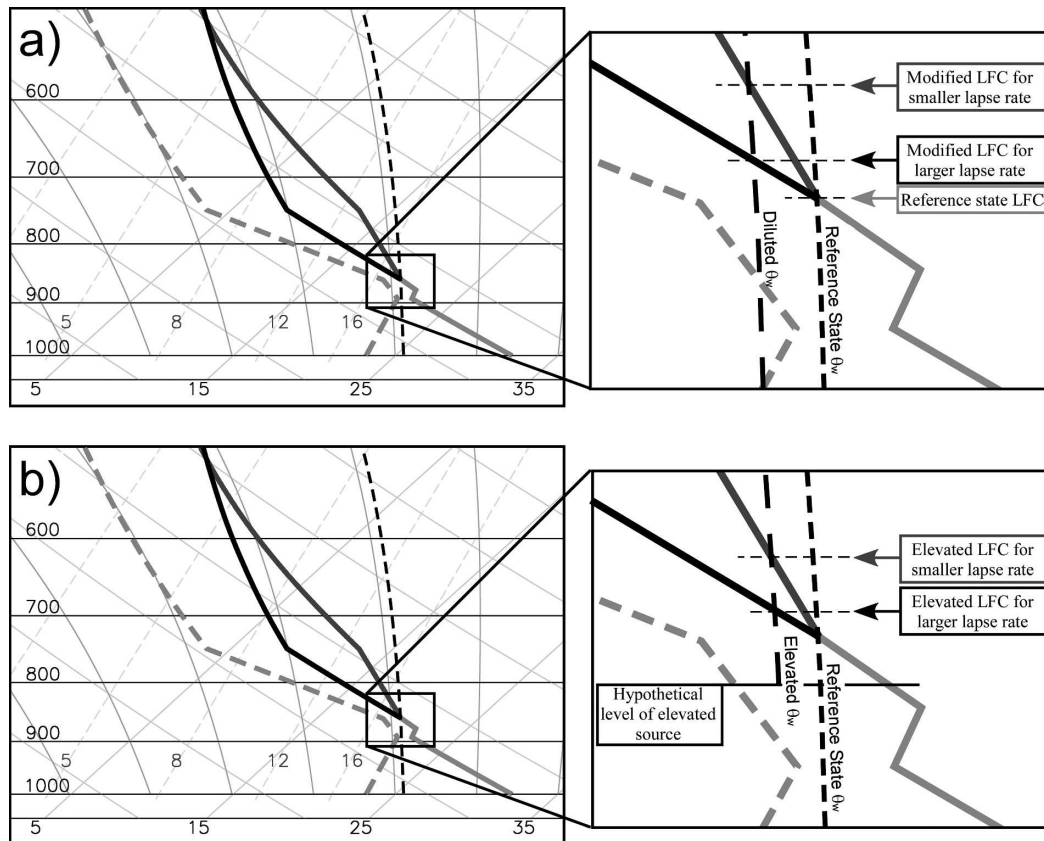E-mail: ahouston2@unl.edu

Fig. 1. Illustration of the possible sensitivity of parcel LFC (and by extension DCI) to the lapse rate of the ACBL for (a) parcels originating in a well-mixed boundary layer and (b) parcels originating in an elevated layer.

by dilution must be lifted higher to be warmer than the environment). When parcel theory is relaxed and the evolutions of individual parcels comprising a convective updraft are considered, deep convective initiation is seen to ultimately depend upon the difference between the depth of forced ascent by the trigger and the diluted, time-dependent LFCs of individual parcels: if the diluted (higher) LFC is greater than the depth of the forced ascent, then DCI will not occur.

Since deep convection can also be initiated from elevated sources (parcels originating above the mixed boundary layer), a robust approach for assessing the likelihood of DCI must also consider this source. Even if dilution is neglected and parcel theory is valid, the use of surface-based or even mixed-layer-based values of CIN and LFC would neglect the possibility that the depth of the forced ascent of *elevated* parcels could exceed their LFCs. By considering the difference between the depth of the forced ascent by the trigger and the LFCs of individual parcels (diluted or not), it is unnecessary to assume a parcel source ex ante facto.

It is only by casting the regulation of DCI in terms of

individual parcels that the possible sensitivity of DCI to the environmental lapse rate of the active cloud-bearing layer can be considered. [The environmental lapse rate is defined as $\Gamma = -\partial T_0/\partial z$, where T_0 is the environmental temperature, and the ACBL is defined as the layer above the LFC, that is, where "active" (Stull 1985) deep convection occurs.] For parcels originating in the planetary boundary layer the increase in the LFC through dilution should be larger for smaller ACBL lapse rates. Consider, for example, two environmental temperature profiles that are identical below a common mixed-layer-based LFC (ML-LFC) but have different lapse rates above this level (Fig. 1a). Dilution of a parcel ascending out of a well-mixed boundary layer will cause the wet-bulb potential temperature (θ_w), which is generally conserved in the absence of mixing, to decrease. This decrease can be driven by the evaporative cooling of cloudy air associated with the mixing of less moist air into the parcel (Ziegler et al. 1997; Ziegler and Rasmussen 1998). This dilution will increase the LFC but the amount of increase will depend on the environmental lapse rate of the ACBL

(Fig. 1a): for a "small" ACBL lapse rate, the environmental temperature above the ML-LFC will be warmer than that for a "large" ACBL lapse rate; thus, a diluted parcel must be lifted higher before it can become positively buoyant. In other words, the diluted LFC will be higher for a smaller lapse rate than for a large lapse rate and DCI less likely.

As with parcels originating in a well-mixed boundary layer, parcels originating in elevated layers should also be characterized by LFCs that are higher for smaller ACBL lapse rates. For two environmental temperature profiles with identical ML-LFCs (Fig. 1b), the moist adiabat (line of constant wet-bulb potential temperature) of an elevated source will intersect the environmental temperature at a higher elevation for a smaller ACBL lapse rate. Thus, the parcel LFC will be higher for a smaller lapse rate. This characteristic would not require parcel dilution.

In an effort to understand the possible sensitivity of DCI to the environmental lapse rate of the ACBL, idealized, cloud-scale, numerical experiments have been conducted in which the response of cloud growth to various environmental lapse rates was tested. Variations in the lapse rates of the reference state (1D) vertical profiles used in the experiments were imposed using an analytical function that ensures constant values of mixed-layer-based CIN (ML-CIN), CAPE (ML-CAPE), LFC, and relative humidity between the different reference states.

Cloud initiation has been simulated in each experiment using a prescribed airmass boundary. While DCI has been attributed to phenomena other than airmass boundaries, the ubiquity of boundary-initiated deep convection (Purdom 1982; Wilson and Schreiber 1986; Wilson and Roberts 2006) suggests that this experimental design will maximize the relevance of the findings. Nevertheless, it is most accurate to interpret the results presented herein as representing the sensitivity of deep convection *initiated on preexisting boundaries* to the environmental lapse rate in the cloud-bearing layer.

The realistic initiation of deep convection in an idealized framework has been particularly challenging in the study of DCI (Ziegler et al. 1997). A method of convective initiation has been developed for this work that we believe satisfies the dual constraints of controllability (necessary for systematically conducting experiments) and realism. An explanation of this method along with a brief description of the numerical model, definition of the experimental suite of analytical reference state environments, and discussion of the limitations of simulated 2D deep convection will follow in section 2. Experimental results and discussion are presented in section 3 followed by conclusions in section 4.

2. Experimental design

a. Model description

All numerical experiments conducted for this work have been performed with the Illinois Collaborative Model for Multiscale Atmospheric Simulations (ICOMMAS). ICOMMAS is a successor to COMMAS (Wicker and Wilhelmson 1995), which has been used extensively in the past for detailed examinations of cloud-scale phenomena (Wicker and Wilhelmson 1995; Wicker et al. 1997; Gilmore and Wicker 1998; Atkins et al. 1999; Peckham and Wicker 2000). The kernel of ICOMMAS is similar in many respects to COMMAS though three primary differences distinguish the two models: (i) the temporal discretization of low-frequency tendencies involves the third-order Runge–Kutta (RK3) method instead of a forward-in-time (Wicker and Wilhelmson 1995) or second-order Runge–Kutta (RK2) (Wicker and Skamarock 1998) scheme; (ii) high-order (≥third order) approximations are used for the spatial discretization of advection instead of the second-order approximation used in the original version of COMMAS; and (iii) the Straka three-phase ice parameterization (Gilmore et al. 2004a) is utilized in lieu of the Kessler or Tao schemes.

ICOMMAS was developed in parallel with L. J. Wicker's development of the National Severe Storms Laboratory version of COMMAS (NCOMMAS; Coniglio et al. 2006) and shares many features. A full description of ICOMMAS is documented by Houston (2004).

As with COMMAS and NCOMMAS, ICOMMAS neglects orography, solar radiation, and surface fluxes of heat and moisture. Furthermore, as is often the case in idealized modeling studies, surface friction is neglected (the lower boundary is free slip). The model domain for all experiments is 40 km long and 20 km deep with a horizontal gridpoint spacing of 100 m and a vertical gridpoint spacing of 50 m stretched to 125 m. The grid spacing used for this work is far too coarse to explicitly treat turbulent kinetic energy dissipation; thus, a version of the 1.5-order closure turbulence parameterization of Klemp and Wilhelmson (1978) is used to approximate the subgrid-scale kinetic energy dissipation. The Klemp and Wilhelmson implementation utilizes a formulation of the prognostic equation for turbulent kinetic energy (TKE) along with flux-gradient theory to predict an eddy-mixing coefficient. Mixing-length theory is then used with this mixing coefficient to close the subgrid-scale transports.

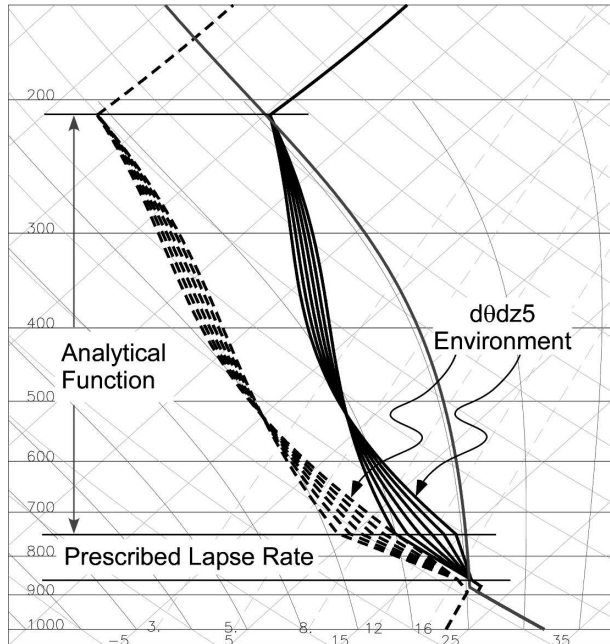The tunable model parameter values used for these experiments are largely the same as the values de-

FIG. 2. Skew T–log$p$ diagram of temperature (continuous black curves) and water vapor mixing ratio (broken black curves) for each of the reference state environments used in the experiment suite.

TABLE 1. Thermodynamic characteristics within the prescribed lapse rate layers for each of the six experiments conducted for this work.

Expt	$d\theta/dz$ (K km^{-1})	$\Gamma = -dT/dz$ (K km^{-1})
dθdz0	0	9.8
dθdz1	1	8.8
dθdz2	2	7.9
dθdz3	3	6.9
dθdz4	4	6.0
dθdz5	5	5.1

scribed by Houston (2004); however, there are two primary differences. The first difference is that the current model setup is 2D. The potential limitations of the 2D framework are reviewed in section 2d. The second difference is in the microphysical parameterization. In the current experiment set, the hail/graupel density and slope intercept are 400 kg m^{-3} and 4×10^8, respectively. These values correspond to the "small graupel" settings used by Gilmore et al. (2004b). A microphysical treatment weighted toward small graupel was chosen because the numerical experiments herein are designed to simulate primarily the early stages of deep convection when significant quantities of large hail are limited.

b. Reference state

A systematic examination of the sensitivity of DCI to lapse rate requires a carefully designed parameter space that isolates the effect of changes in lapse rate from other environmental characteristics that can modulate DCI. To this end, a technique was designed to analytically generate vertical profiles of temperature, moisture, and winds.

The reference state in ICOMMAS is horizontally homogeneous and is imposed by introducing a reference state "sounding" containing the vertical distributions of the temperature, moisture, and winds. Six soundings are used and are illustrated in Fig. 2. *The temperature*

and moisture profiles of these soundings are identical below the ML-LFC at 1320 m and include an inversion between 1000 m and the ML-LFC that yields approximately 5.1 J kg^{-1} of ML-CIN.

Lapse rate variations between the soundings of the experiment set are imposed through modification of the temperature profile above the common ML-LFC. In each sounding, the prescribed lapse rate occupies the layer between the ML-LFC and 2500 m. Values of $d\theta_0/dz$ for these soundings range from 0 to 5 K km^{-1} (which correspond to lapse rates ranging from 9.8 to 5.1 K km^{-1}). A summary of the six experiments that compose the experiment set appears in Table 1. Note that the experiment name refers to the value of $d\theta_0/dz$ within the prescribed lapse rate (e.g., dθdz0 corresponds to a value of $d\theta_0/dz$ equal to 0 within the prescribed lapse rate layer).

To ensure identical values of ML-CAPE and tropopause height across all vertical profiles, the temperature profile above the prescribed lapse rate layer is defined by prescribing the vertical distribution of buoyancy using an analytical function that relates the ML-CAPE within the prescribed lapse rate layer (which will vary for each sounding) to the predefined total ML-CAPE of the sounding. The total ML-CAPE for all soundings is fixed at a value of 2500 J kg^{-1}. A full description of the approach is included in appendix A.

The profiles of moisture for each environment are determined after the prescription of temperature and are set to insure that the relative humidity above the ML-LFC is the same for each environment.[1] As indicated in Fig. 2, the θ_w value within the cloud-bearing layer below ~5300 m is anticorrelated with the lapse rate of the ACBL. This source of low-θ_w air could increase the magnitude of cloud dilution and thereby

---

[1] For simplicity, the analytical buoyancy is computed without accounting for the effects of moisture on density. Such effects are most significant in the low levels of the atmosphere where the amount of moisture is largest. Since the reference state thermodynamics below the ML-LFC are identical between soundings used in this work, neglecting moisture in the buoyancy has little effect on the CAPE.
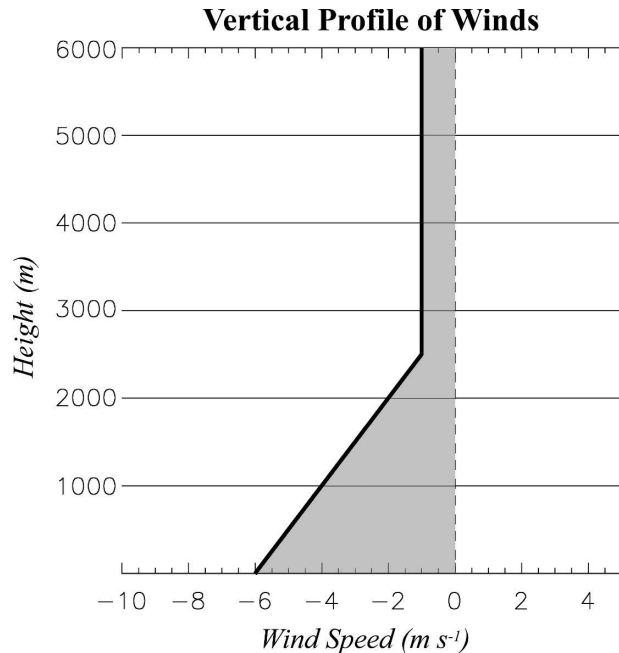
Vertical Profile of Winds

FIG. 3. Vertical profile of reference state winds used for all experiments.

TABLE 2. Parameter values common to each environment used in these experiments.

Parameter		Value
Total CAPE of final sounding	E_{tot}	2500 J kg^{-1}
"Boundary layer" potential temperature		305 K
CIN		5.1 J kg^{-1}
Height of the tropopause (top of the analytical layer)	z_t	12 000 m
Top of the prescribed lapse rate layer	z_m	2500 m
Top of the layer with vertical wind shear		2500 m
Relative humidity at the top of the prescribed lapse rate layer		70%
Relative humidity at the tropopause		20%
Magnitude of the nonzero vertical wind shear		2×10^{-3} s^{-1}

mitigate the hypothesized increased likelihood of DCI in the higher lapse rate environments.

The vertical profile of wind velocity is the same for all soundings and is illustrated in Fig. 3. Positive vertical shear ($du/dx > 0$) was included in the reference state winds because of the well-documented correlation between the depth–magnitude of forced ascent at airmass boundaries and the vertical shear (e.g., Rotunno et al. 1988; Xu 1992; Liu and Moncrieff 1996; Xu et al. 1996; Xue et al. 1997; Weisman and Rotunno 2004). The value for the vertical wind shear was chosen so that the environment would not possess a steering level (a level at which the airmass boundary-relative winds are zero). This ensured that clouds developing at the boundary would be transported rearward of the boundary. The imposed vertical wind shear vector was directed toward the east and had a magnitude of 2×10^{-3} s^{-1}. This wind shear magnitude is well below that which would be expected for supercells. Because of the inherent three-dimensionality of supercells, a more robust comparison can be made between the 2D deep moist convection modeled in this work to real deep moist convection in environments that are not supercellular. A summary of the parameters shared by all six experiments of the control experiment set are listed in Table 2.

c. Preexisting airmass boundary initialization

Deep convection is traditionally initiated in idealized cloud models with a thermal bubble: a localized region in which the temperature and/or moisture are perturbed so as to locally release thermal instability. While inherently unrealistic, this method is usually satisfactory when the perturbation is small and when the focus of the analysis is on the character of deep convection several convective time scales following initiation. However, when the focus of the analysis is on initiation, the thermal bubble is inappropriate (Ziegler et al. 1997).

Alternatives to the thermal bubble in idealized cloud-scale models have generally relied upon airmass boundaries to initiate deep convection. In these approaches, the mechanical lifting and/or a solenoidal circulation along the imposed boundary trigger deep convection. Previous methods can be loosely categorized as either ad hoc initializations in which the temperature, moisture, and/or wind field are explicitly imposed (e.g., Hane 1975; Lee and Wilhelmson 1997; Atkins et al. 1999; Peckham et al. 2004) or forcing initializations in which temperature, moisture, and/or wind velocity heterogeneities are created gradually via a tendency term (e.g., Dudhia and Moncrieff 1989). Both categories of initialization can be criticized for lack of realism but, as with the thermal bubble initialization, such deficiencies can largely be ignored when the focus of the analysis is on the character of the simulated deep convection well after initiation.

A preexisting boundary has been chosen for the initiation of deep convection in these experiments. DCI is frequently attributed to airmass boundaries (Purdom 1982; Wilson and Schreiber 1986; Wilson and Roberts 2006) and thus this mechanism has broad applicability to the study of deep convective initiation.

The preexisting airmass boundary used for these experiments is initialized as a density current. The vertical structure of a density current (e.g., the depth, magnitude of ascent, etc.) is dependent on the vertical wind shear (Xu 1992; Liu and Moncrieff 1996; Xu et al. 1996; Xue et al. 1997) and static stability (Liu and Moncrieff
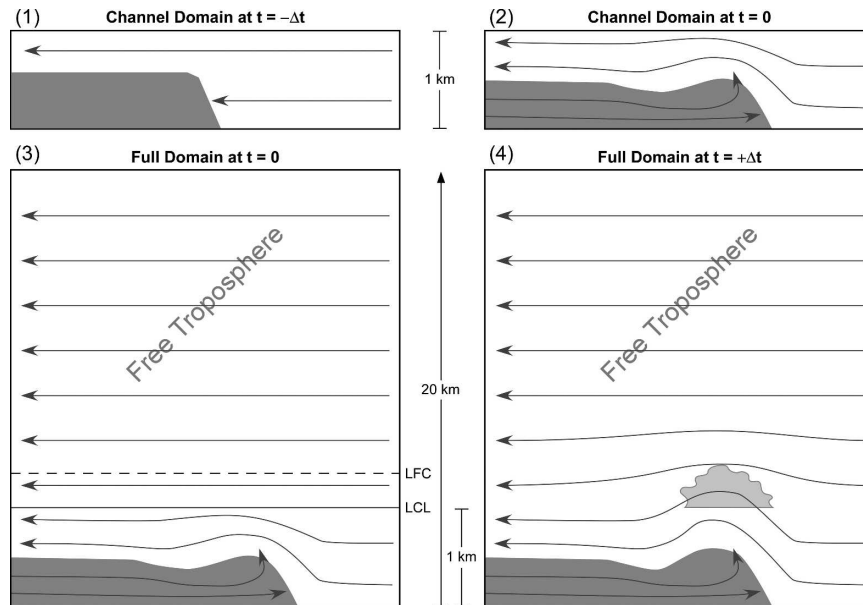
FIG. 4. Conceptual illustration of the airmass boundary initialization ("seeding") technique utilized in this work. Each panel represents a step in the procedure.

2000; Xue 2002) of the reference state environment upstream of the density current. In these experiments the vertical shear and static stability of the well-mixed layer within which the shallow density current resides are the same for all environments; thus, the vertical structures of the simulated preexisting boundaries should be as well.

The preexisting boundary is initialized as a perturbation to the 1D (stratified) reference state potential temperature and wind velocity. The initial block is 550 m deep and covers the western 10 km of the domain. The air mass within the block is initially static and 4 K colder than the reference state conditions.

The model's state variables will vigorously adjust to the imposed boundary. This initial adjustment to the block is unrealistic: a block of cold air does materialize suddenly like this in the actual atmosphere. This adjustment has the potential to produce an unrealistic treatment of convective initiation. To obviate this threat to the realism of the initialization method, this adjustment should occur prior to, and independent from, convective initiation along the boundary. To meet this requirement, a technique has been developed that simulates the adjustment process separately from the simulation of convective initiation.

The key element of this technique is to simulate the preexisting boundary in a shallow (channel) domain prior to introducing the preexisting boundary into the full domain. (The shallow domain can be thought of as a strongly capped boundary layer.) Since the domain captures the portion of the reference environment be-

low the LCL, cloud formation is not allowed and because of the reflective upper boundary condition, the flow is purely lateral at the upper boundary. Thus, when the preexisting boundary and its attendant flow field are introduced into the larger domain, the vertical velocity fields at and above the LCL and LFC are able to gradually respond to the preexisting boundary. In other words, *the vigorous adjustment of the model's state variables is disassociated from the simulation of convection.*

The specific steps in the technique are illustrated in Fig. 4 and are as follows. (i) The block of cold air is initialized in the channel domain. (ii) The model state variables are allowed to adjust within the channel domain for 3600 s. (iii) The temperature and momentum fields associated with the "adjusted" preexisting boundary are used to "seed" the full domain simulation. As illustrated in Fig. 4 and in the results presented in section 3, the time that the seed is introduced into the full domain is treated as the initial time ($t = 0$). (iv) Additional (gradual) adjustment to the preexisting boundary produces a forced cumulus cloud and the potential for active convection. Because the lowest 1000 m of all reference state environments used in the control experiment suite are identical, *the same seed is used for each experiment.*

Adjustment of the model's state variables will occur in response to any changes to the density or wind fields within the air masses on either side of a boundary. However, the *vigorous* adjustment that this technique aims to manage is an artifact of initializing the bound-
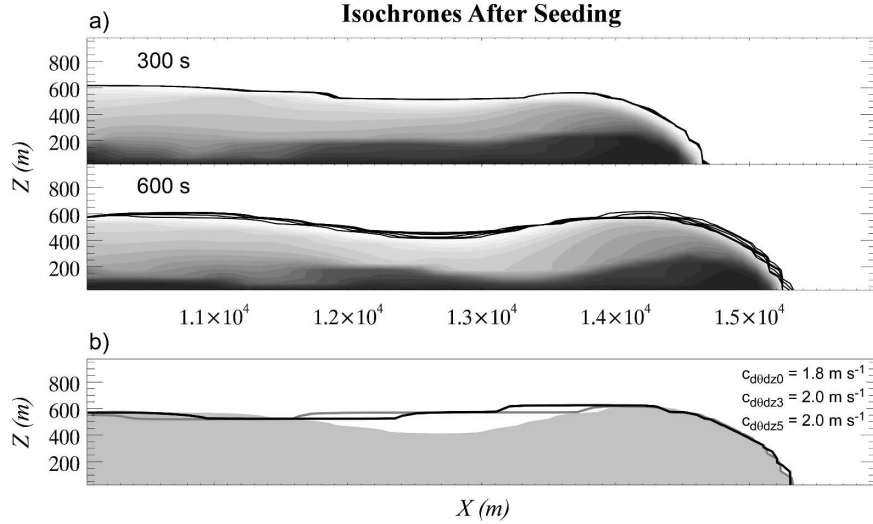
FIG. 5. (a) Isochrones (defined as the 0-K θ' contour) for the preexisting boundaries simulated in each of the six experiments at 300 and 600 s after seeding (3900 and 4200 s, respectively). The θ' field for the dθdz0 experiment is shaded at an interval of 0.2 K. (b) Isochrones for the dθdz3 experiment at 2400 s (black curve) and the dθdz5 experiment at 3600 s (gray curve) along with the region of $\theta' < 0$ K for the dθdz0 experiment (shaded). The boundary translation speeds at 600, 2400, and 3600 s for the dθdz0, dθdz3, and dθdz5 experiments, respectively, appear in the top-right corner of the panel.

ary with a block of cold air. There are other methods for initializing the air mass on the cold side of the boundary that would avoid this initial unrealistic adjustment. One such method is the heat sink (e.g., Dudhia and Moncrieff 1989; Garner and Thorpe 1992; Fovell and Tan 2000). In this method the air mass on the cool side of the boundary is slowly introduced by cooling a region of the atmosphere in contact with the surface. This approach can be thought of as simulating the evaporative cooling associated with precipitation or the reduction in insolation due to cloud cover. However, while bearing similarities to atmospheric processes, *the heat sink method makes no attempt to achieve a quasi-steady-state boundary prior to DCI.* Thus, if, as in the simulations conducted for this work, DCI occurs at different times in each experiment, there is no way to ensure that the structure of the boundary is being controlled for. However, in the method used here, not only is the initial unrealistic adjustment of the block isolated from DCI, but by allowing the boundary to evolve for 1 h before introducing the seed into the full domain, this method also ensures a quasi-steady-state boundary and thus controls for variations in boundary structure.

The steadiness of the simulated boundaries is illustrated with X–Z isochrones in Fig. 5. It is clear that 1) the classic density current structure is captured by the initialization procedure and 2) the structural differences between the density currents are very small. The latter (qualitative) observation is further supported (quantitatively) by noting that the difference between the density current depths of the largest and smallest lapse experiments is ~25 m after 600 s of integration. This difference is only 4% of the density current depth. Furthermore, as it will be shown in section 3, thermal instability release is delayed for more than 2400 s following the introduction of the seed in the dθdz3 experiment. Yet, as illustrated in Fig. 5b, the structure and translational speed of the density current remains virtually unchanged throughout the simulation. In the dθdz5 experiment, for which thermal instability is never released, the density current structure and translational speed remain quasi-steady through the entire simulation.

While this initialization mechanism clearly captures the essence of airmass boundaries that behave as density currents, the omission of heterogeneous surface fluxes of heat and moisture will neglect the planetary boundary layer secondary circulations that can play a role in DCI (refer to the review of Weckwerth and Parsons 2006). However, such boundary layer processes are not necessary for DCI.

d. 2D versus 3D simulations of deep convection

Real deep convection is rarely slab-symmetric (two-dimensional) so there will undoubtedly be some loss of generality using a 2D model framework. Comparisons between 2D (rectilinear) and 3D (either axisymmetric or fully 3D) convection have consistently demonstrated
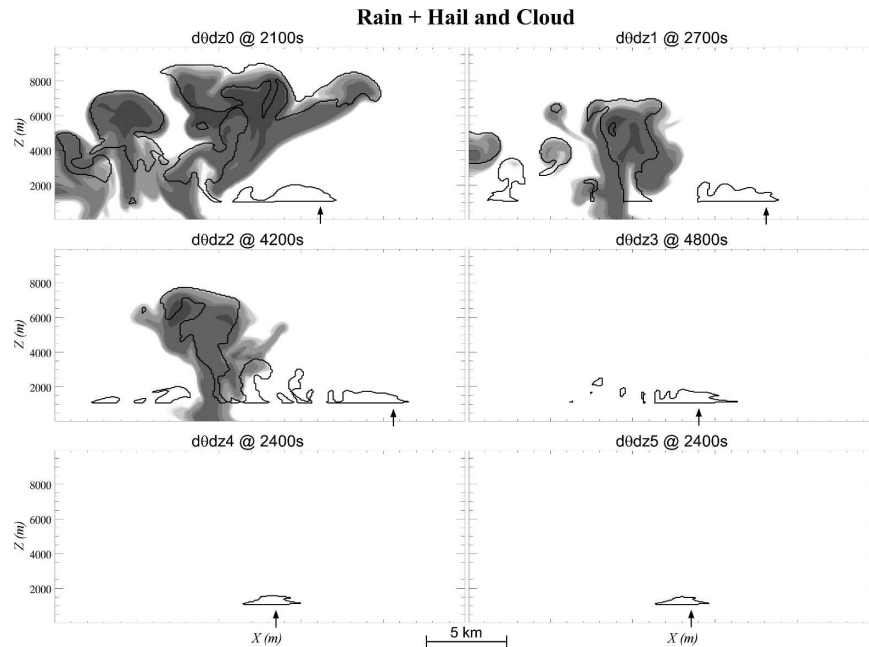
Rain + Hail and Cloud

FIG. 6. Precipitation and cloud fields for the six experiments. Precipitation (the combined mixing ratios of rainwater and hail/graupel) is shaded at a logarithmic interval of 5×10^{-n} kg kg^{-1} from a minimum value of 5×10^{-7} kg kg^{-1}, and the 5×10^{-8} kg kg^{-1} mixing ratio isopleths of the total cloud (the combined mixing ratios of cloud water and cloud ice) are contoured. Vertical black arrows indicate the position of the preexisting boundary. All times are the elapsed times since the introduction of the seed into the full domain.

several limitations of 2D simulations that might be relevant to the experiments conducted for this work.

Midlevel downdrafts on the flanks of a growing cloud and driven by the cloud's buoyant circulation are considerably stronger in 2D clouds (Ogura 1963; Murray 1970; Schlesinger 1984). This disparity is a direct consequence of the unrealistically small area that the downdraft is confined to occupy in 2D. As argued by Schlesinger (1984), if the updraft occupies a given fraction σ of the total cell width, then the ratio of downdraft-to-updraft areas in 2D is a factor of $\sigma/(1 + \sigma)$ smaller than the downdraft-to-updraft area ratio in axisymmetric coordinates. The compressional warming and drying associated with this "compensating" downdraft in place just outside of the updraft has the potential to decrease the thermal buoyancy within the cloud and exaggerate the erosion of the cloud column through entrainment (Schlesinger 1984). This cloud column erosion can yield a 2D cloud shaped like a mushroom in situations where no such structure is apparent in 3D (Murray 1970). Given that convective initiation is intimately tied to processes occurring in the early stages of cloud growth, this characteristic of 2D simulations must be considered when interpreting the results from the experiments performed for this work.

Despite these limitations of the 2D framework, 2D simulations of deep convection have been used extensively over the last 10 yr (e.g., Fovell and Dailey 1995; Fovell and Tan 1998; Lin et al. 1998; Bryan and Fritch 2002; Xue 2002; Bryan 2005). In particular, the work of Fovell and coauthors and Lin and coauthors has treated the development of deep convection on airmass boundaries. And while their airmass boundaries were storm generated (not preexisting), their results clearly demonstrated that the 2D framework could capture the initiation of deep convection.

3. Results and discussion

Of the six simulations conducted for the experiment set, only the three environments with the largest lapse rates support DCI.[2] Snapshots of the cloud and precipitation for these six experiments are provided in Fig. 6 (all times listed in this figure and elsewhere in this article are the elapsed times since the introduction of the seed into the full domain). Shallow clouds are simulated at the preexisting boundary in the environments with the three smallest lapse rates but DCI is inhibited through the duration of these simulations.

―――――――

[2] DCI is defined for this work as moist convection that produces precipitation at the surface.
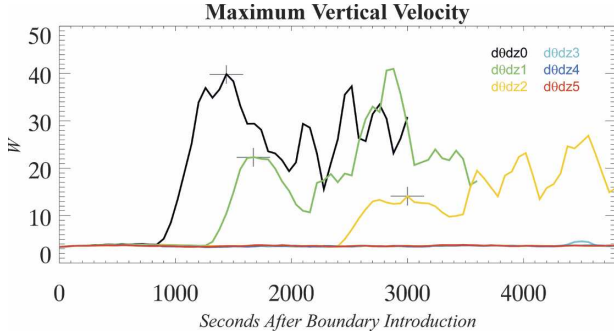
Maximum Vertical Velocity

FIG. 7. Time series of domain-maximum vertical velocity values for the six experiments. Crosshairs on the dθdz0, dθdz1, and dθdz2 experiments indicate the maximum vertical velocity for the first deep convective cloud of the experiment.

TABLE 3. Values of wet-bulb potential temperature (K) surfaces chosen for the seven heights for each of the six experiments.

Surface height (m)	dθdz0	dθdz1	dθdz2	dθdz3	dθdz4	dθdz5
1000	298.6	298.6	298.6	298.6	298.6	298.6
1100	298.5	298.5	298.5	298.5	298.5	298.5
1200	298.3	298.3	298.3	298.3	298.3	298.3
1300	298.0	298.0	298.0	298.0	298.0	298.0
1400	297.4	297.4	297.5	297.6	297.6	297.7
1500	296.7	296.8	297.0	297.1	297.3	297.4
1600	296.0	296.2	296.5	296.7	296.9	297.2

Time series plots of the domain-maximum vertical velocity values (Fig. 7) show that, among the environments that supported DCI, the time required for initiation decreases with increasing lapse rate. Furthermore, the magnitude of the maximum vertical velocity value for the initial deep convection clearly increases with increasing lapse rate.

In general, there are two possible explanations for the simulated sensitivity of DCI to lapse rate: 1) air parcels are less likely to reach their LFC for smaller lapse rate environments or 2) air parcels reach their LFC (thermal instability is released) but the resultant shallow convection becomes diluted prior to maturation for smaller lapse rate environments. Section 3a will treat the former possibility and section 3b will treat the latter.

a. Dependence of parcel ascent to the LFC on lapse rate

In these experiments, if air parcels are more likely to reach their LFC in the larger lapse rate environments, it is because the forced ascent at the preexisting boundary is stronger and/or the parcels' LFCs are lower (as proposed in section 1). The following subsections address these two possibilities.

1) INTEREXPERIMENT VARIATIONS IN FORCED ASCENT

The assumption underpinning the hypothesized role of LFC height in regulating DCI between environments with differing ACBL lapse rates (section 1) was that the depth of the forced ascent was independent of the lapse rate. However, in 2D idealized density current experiments, Xue (2002) found that the depth of the forced ascent at the leading edge of a density current (as well as the depth of the density current itself) was negatively

correlated with the lapse rate in an overlying inversion. Thus, it is possible that identical initial preexisting boundaries can produce differing depths of forced ascent if only the overlying lapse rates are different.

To examine the differences in forced ascent in these experiments, we consider the upward displacement of wet-bulb isentropic (θ_w) surfaces. This method was chosen in place of trajectory analysis because the deflection of θ_w surfaces captures the cumulative effect of parcel displacement. Since the vertical profiles of θ_w differ above the LFC between experiments, the same surfaces could not be used for all experiments and all heights. Instead, a suite of heights was chosen and the θ_w surfaces in each environment that corresponded to these altitudes were identified (see Table 3 for a summary of the θ_w values used for each of the seven heights). Analysis of the vertical displacement of these surfaces was undertaken prior to the release of thermal instability in any of the experiments. After this time, surface displacement could have been the result of positively buoyant motions as well.

The displacement of the chosen surfaces is illustrated in Fig. 8. The black (gray) curves represent the surfaces of the dθdz0 (dθdz5) experiment. The corresponding surfaces for the remaining experiments reside within the shaded envelopes between the dθdz0 and dθdz5 curves and are distributed monotonically within these envelopes. It is clear that the forced ascent at the preexisting boundary increases with increasing ACBL lapse rate. Figure 9 provides a more quantitative assessment of the displacements of the θ_w surfaces. From this figure it is also clear that while the magnitude of the displacement is largest for the lower isentropic surfaces (e.g., the 1000-m isentropic surface in the dθdz0 experiment is displaced 165 m but the 1600-m surface is displaced only 104 m), the interexperiment differences between the surface displacements are largest for the upper isentropic surfaces (e.g., the difference in the displacement of the 1000-m surface between the dθdz0 and dθdz1 experiments is 10 m but is 10.6 m for the 1600-m surface). Consistent with this finding, the larg-
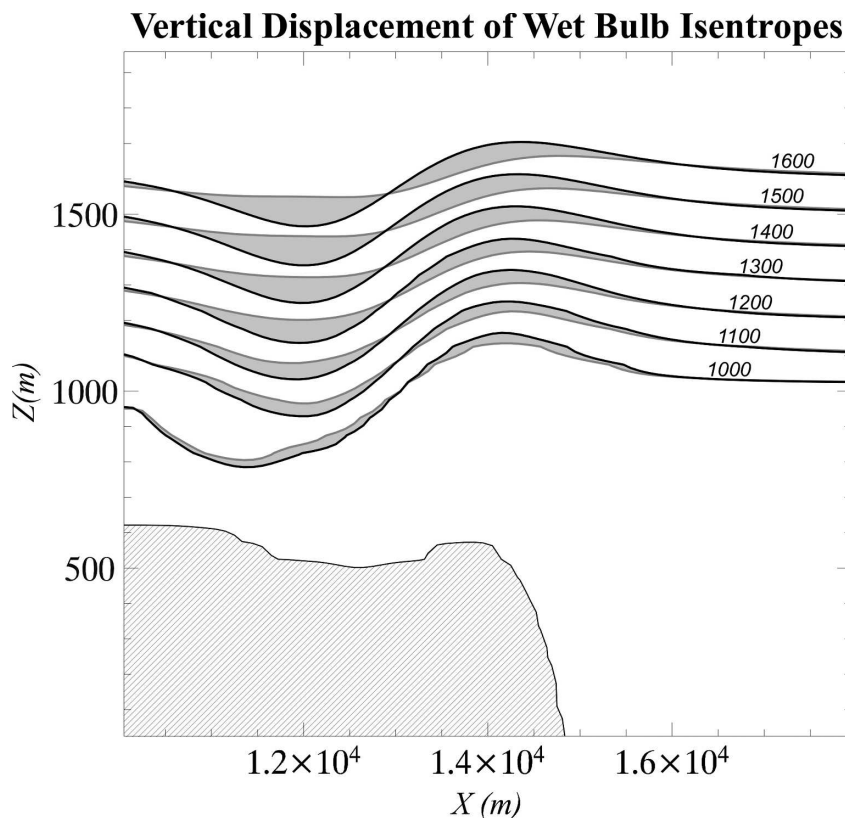
Vertical Displacement of Wet Bulb Isentropes

FIG. 8. Vertical displacement of wet-bulb potential temperature (θ_w) surfaces by forced ascent in the dθdz0 and dθdz5 experiments at 360 s. The initial heights (m) of each surface are indicated with italicized numbers. The surfaces for dθdz0 (dθdz5) appear as black (gray) curves. The gray envelopes represent the regions within which the corresponding surfaces for the remaining experiments reside. The hatched region represents the density current for the dθdz0 experiment.

est differences in upward motion between the dθdz0 and dθdz5 experiments (Fig. 10) appear in the 1500–2000-m layer in the presence of *unsaturated* ascent. Within this layer, the negative buoyancy force for unsaturated motions will be smaller in magnitude for larger lapse rates. Thus, the differences in forced ascent are directly attributable to differences in the ACBL lapse rates between experiments.

The foregoing analysis reveals that, even though density current depths vary little between experiments, the magnitude/depth of the forced ascent is clearly positively correlated with the lapse rate of the cloud-bearing layer. But were these differences in the forced ascent sufficient to explain the failure of DCI in the three smallest lapse rate environments? If they were sufficient, then DCI should be prevented in the (large lapse rate) experiments that previously supported DCI by simply replacing the forced ascent in these experiments with the smaller forced ascent of the (small lapse rate) experiments that did not support DCI. While it is

impossible to conduct these proposed experiments in a numerical modeling framework, the results of such experiments can be estimated by comparing two quantities: 1) the vertical displacement (Δz) of each of the seven θ_w surfaces considered previously (Table 3) for the dθdz4 and dθdz5 experiments (at 7200 s) and 2) the distance each representative θ_w surface of the dθdz0, dθdz1, and dθdz2 environments would have to be vertically displaced from their reference heights to release thermal instability (i.e., Δz_k^* for,

$$\Delta z_k^* = \mathrm{LFC}_{Z_k} - Z_k, \tag{1}$$

where Z_k is the kth reference height and LFC_{Z_k} is the LFC for parcels lifted from Z_k). Experiments dθdz4 and dθdz5 are used for Δz because they not only failed to produce deep convection but also failed to release thermal instability through 7200 s. These quantities are plotted in Fig. 11 and illustrate that the vertical displacement of the isentropic levels originating between
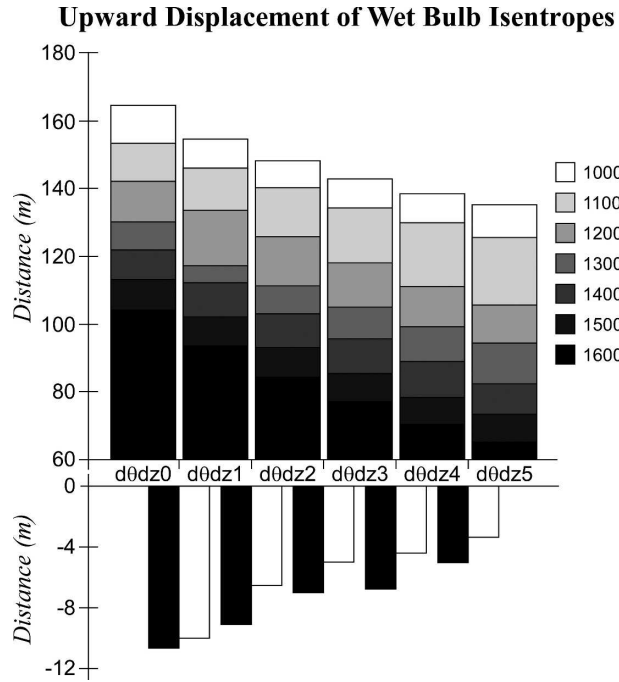
Upward Displacement of Wet Bulb Isentropes

FIG. 9. (top) Upward displacement (in m from the reference height) of θ_w surfaces by forced ascent in the six experiments at 360 s. (bottom) Interexperiment differences in vertical displacement for the θ_w surfaces originating at 1000 and 1600 m.

~1200 and ~1400 m in the dθdz4 and dθdz5 experiments exceeds the displacements necessary to release thermal instability in the dθdz0 and dθdz1 experiments ($\Delta z > \Delta z_k^*$ for $1400 > k > 1200$). Thus, replacing the larger displacements of the dθdz0 and dθdz1 experiments with the smaller displacements of the dθdz4 and

dθdz5 experiments would still have likely released thermal instability (the weaker forced ascent was still sufficient to lift parcels to the LFC) and would have probably still yielded DCI. Therefore, the sensitivity of forced ascent to the ACBL lapse rate is not a *sufficient* explanation for the sensitivity of DCI to the ACBL lapse rate.

While not a sufficient explanation, the sensitivity of forced ascent to the ACBL lapse rate cannot be neglected when taking full account of the sensitivity of DCI to the ACBL lapse rate. For example, as illustrated in Fig. 11, $\Delta z < \Delta z_k^*$ for the dθdz2 experiment; thus, reducing the upward displacement would have presumably prevented DCI in this experiment.

2) INTEREXPERIMENT VARIATIONS IN PARCEL LFC

As discussed in section 1, the precise nature of the sensitivity of parcel LFCs to the ACBL lapse rate will depend on the source of air within the convective clouds. If the source of air resides in the lowest 1000 m in these experiments, then θ_w dilution within cloudy air is necessary to realize interexperiment differences in the LFC. However, if the source or air resides above 1000 m in these experiments, the LFC will be different even in the absence of dilution.

To identify the source of air within the simulated deep convection, collections of weightless trajectories were initiated within the cloudy and positively buoyant air at 60-s intervals during the first 20 min after thermal instability was first released. These trajectories were then backward integrated to the beginning of the simulations using fourth-order Runge–Kutta temporal dif-
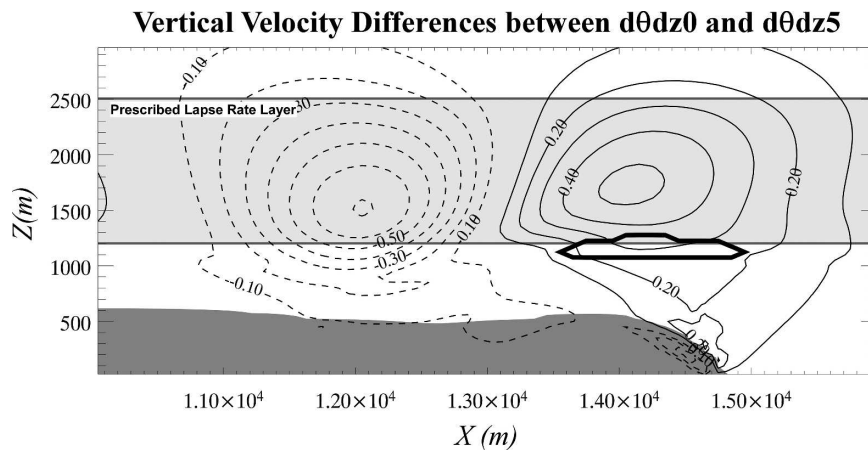
Vertical Velocity Differences between dθdz0 and dθdz5

FIG. 10. Difference between the vertical velocity values of the dθdz0 and dθdz5 experiments at 360 s. Thin black contours represent $w_{\text{d}\theta\text{dz0}} - w_{\text{d}\theta\text{dz5}}$ contoured every 0.1 m s^{-1} (broken contours are for values less than zero). Gray shaded region at the lower boundary represents the cold air behind the preexisting boundary of the dθdz0 experiment. The cloud from the dθdz0 experiment is indicated by the thick black curve.
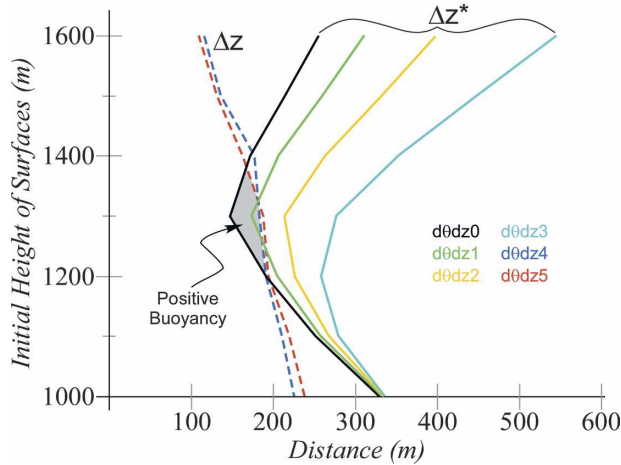
FIG. 11. Comparison of the vertical displacement of the wet-bulb isentropic surfaces in the dθdz4 and dθdz5 experiments (Δz) to the distance each representative wet-bulb isentropic surface of the dθdz0, dθdz1, and dθdz2 environments would have to be vertically displaced from their reference heights to release thermal instability (Δz^*).

ferencing at a primary time step of 15 s and an intermediate time step of 5 s. Histograms of source regions were then synthesized for each of the experiments that yielded DCI. Histograms for the dθdz0, dθdz1, and dθdz2 experiments appear in Fig. 12.

In all three experiments, deep convection was initiated from parcels originating above 1000 m. The peak contribution came from parcels originating near 1300 m. In fact, for the first 420, 840, and 1740 s of positive buoyancy for the dθdz0, dθdz1, and dθdz2 experiments, respectively, no parcels in the cloudy regions of positive buoyancy originated below 1000 m. Parcels that originated below 1000 m in the early stages of the convective clouds and managed to ascend above their LCL, passed through the cloudy region at and behind the preexisting

boundary, underneath the region of positive buoyancy, and became diluted before thermal instability could be released. However, as the convective cloud matured and upward motion increased, some of these saturated parcels were drawn into the developing cloud and became buoyant. This behavior manifested as a split flow and is illustrated in Fig. 13. Parcels that originated above 1000 m (green trajectories in Fig. 13) ascended within the buoyant cloud while parcels below 1000 m (blue trajectories in Fig. 13) followed flat if not descending tracks after passing over the preexisting boundary but were then ingested into the cloud.

This pattern of convective initiation is very similar to the DCI simulated by Fovell (2005). In his simulations of horizontal convective rolls and sea-breeze fronts, the first release of thermal instability occurred in parcels originated above the mixed layer. Parcels originating within the mixed layer contributed to the cloud only later when the convection was more fully developed.

If the simulated forced ascent was larger at 1000 m than it was above this level (Fig. 9), why is thermal instability released first in parcels originating above 1300 m? Note from Fig. 11 that the value of Δz^* was smallest at 1300 m in the three experiments that produced deep convection. Thus, while the upward displacement was larger at (and presumably below) 1000 m, the vertical displacement that was necessary for the release of thermal instability was actually smaller in the ~600 m above this point and was smallest at 1300 m, the level from which the largest percentage of buoyant parcels originated.

It is important to reiterate that, *despite the presence of a surface-based boundary*, deep convection was initiated from elevated sources. The *Glossary of Meteorology* defines "elevated convection" as "convection that originates from an atmospheric layer above the boundary layer." While the convective clouds of these
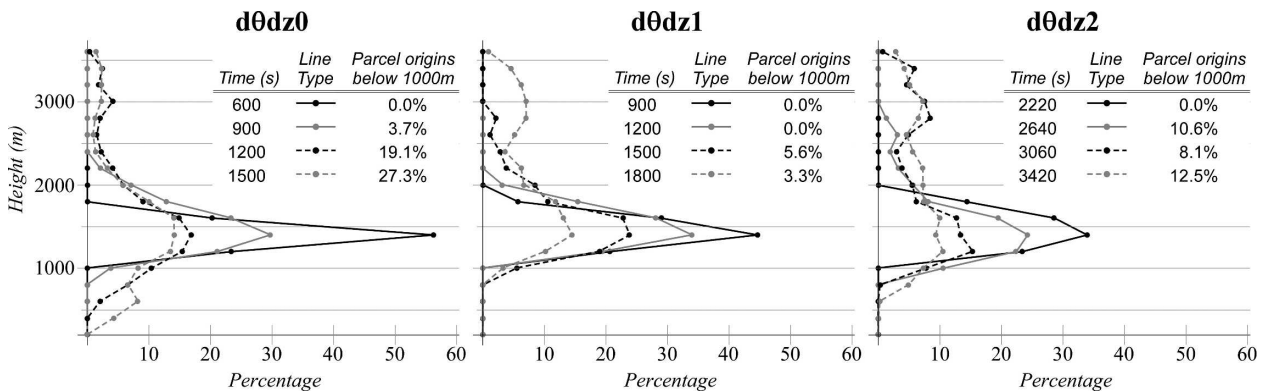

FIG. 12. Histograms of parcel sources for experiments dθdz0, dθdz1, and dθdz2. Height bins are in 200-m increments. Percentage below 1000 m is computed for the parcels originating between 0 and 2500 m.
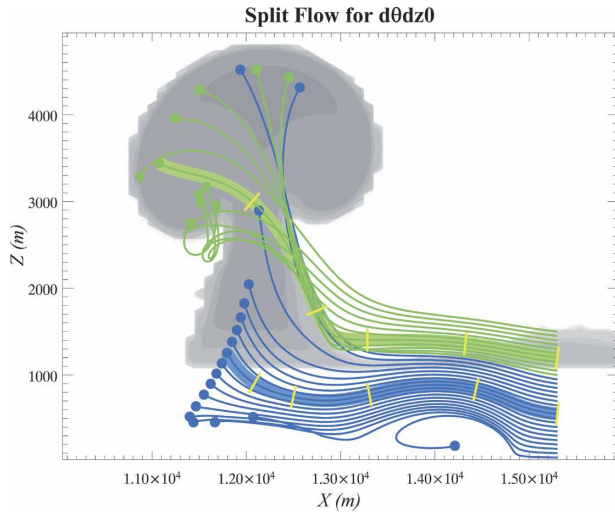
FIG. 13. Cloud field at 1200 s and trajectories forward integrated from 240 s for the dθdz0 experiment. Trajectories originating above (below) 1000 m appear in green (blue). Trajectory positions at 1200 s appear as filled circles. The thick curves are representative trajectories in the two airstreams. Hatches along these representative trajectories are the trajectory positions every 192 s.

experiments did initiate from sources above the well-mixed layer below 1000 m, to describe them as elevated convection would be misleading since there was a significant contribution from low-level sources following initiation. The term elevated convection is also often associated with convective clouds with cloud bases above the ML-LCL, and while this is an informal definition only, it is not the case in these simulations since the active portions of the nascent deep convective clouds at the time of initiation surmount a forced cloud with a base at the ML-LCL (Fig. 14).

Based on the relationship between parcel LFC and ACBL lapse rates offered in section 1, the fact that simulated deep convection was initiated from elevated sources means that interexperiment differences in parcel LFCs that led to DCI failure in experiments dθdz4 and dθdz5 (for which no parcel ascended above its LFC) did not require dilution, as would have been the case if convective clouds were initiated from air in the lowest 1000 m. Instead, as illustrated in Fig. 15, the LFCs for elevated sources differ strictly as a result of differences in the ACBL lapse rates: the LFCs are lower in the larger ACBL lapse rate environments for air lifted from between 1000 and ~2000 m.

LFCs for elevated sources are clearly a function of the ACBL lapse rates but are these differences a sufficient explanation for the observed sensitivity of DCI to lapse rate? Based on the thought experiment of section 3a(1), forced ascent alone could not explain the sensitivity of DCI to the ACBL lapse rate but, given that $\Delta z < \Delta z_k^*$ for the dθdz2 experiment (see Fig. 11), neither could it be neglected. Therefore, air parcels were more likely to reach their LFCs in the experiments with larger ACBL lapse rates because the forced ascent at the preexisting boundary was stronger *and* because the parcels' LFCs were lower, irrespective of parcel dilution.

b. DCI failure in the presence of thermal instability release

Like the dθdz4 and dθdz5 experiments, the dθdz3 experiment failed to support DCI through 7200 s of simulation time following the introduction of the "seed." However, unlike dθdz4 and dθdz5, the dθdz3 experiment did release thermal instability (Fig. 16). The
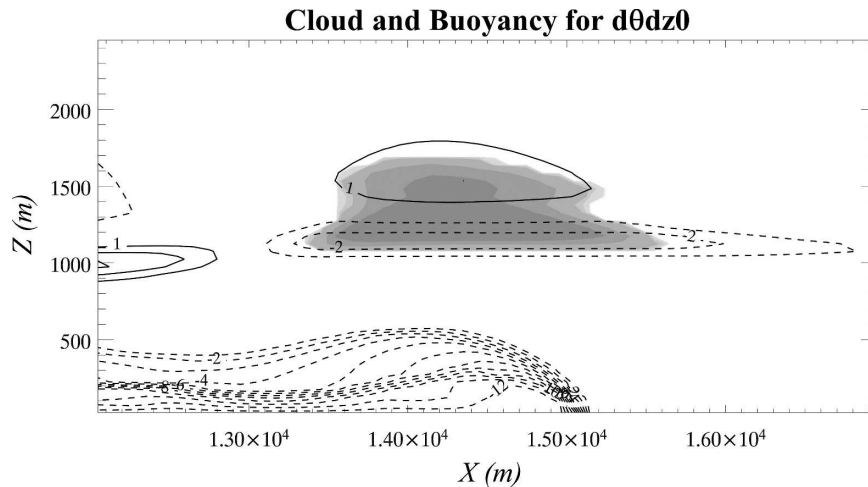

FIG. 14. Cloud and buoyancy for dθdz0. Total cloud (cloud ice plus cloud water) is shaded at a logarithmic interval of 5×10^{-n} kg kg^{-1} from a minimum value of 5×10^{-7} kg kg^{-1}. Buoyancy is contoured every 1×10^{-2} m s^{-2} (negative values appear as broken contours).
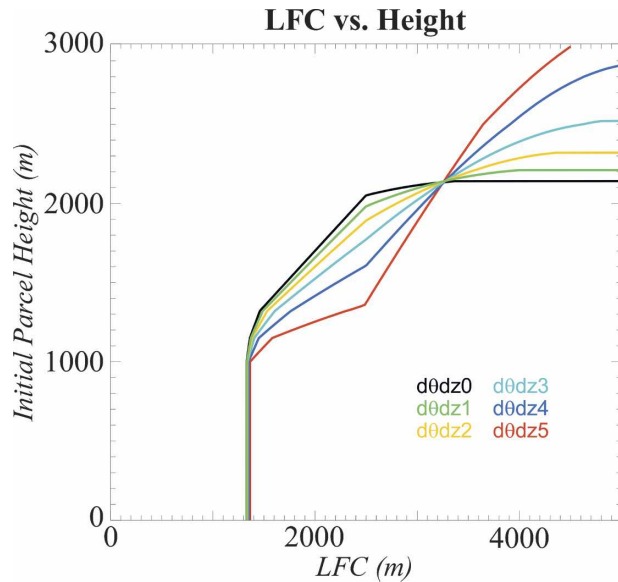
FIG. 15. LFC as a function of the height from which air is lifted for each of the environments used in these experiments.

resultant shallow convective clouds became diluted before producing precipitation. Thus, while DCI failure in the dθdz4 and dθdz5 experiments could be attributed to the failure of parcels to ascend to their LFCs, a similar explanation cannot be used to explain DCI failure in the dθdz3 experiment.

Environments with constant lapse rates, as in the prescribed lapse rate layers used in these experiments, are examples of classic thermal instability wherein the vertical displacement produced by positive (negative) buoyancy acts, nonlinearly, to increase (decrease) the buoyancy and yield larger vertical displacement. However, if the buoyancy is reduced or the buoyant acceleration is mitigated by processes that increase the magnitude of the downward-directed pressure gradient force, then upward parcel displacement will be suppressed and it may not be possible to fully realize the thermal instability. In the absence of significant precipitation and other mitigating forces, changes in buoyancy due to parcel mixing/dilution will have be the most significant influence on regulating the full release of the thermal instability.

The maximum values of positive buoyancy within the primary simulated convective clouds (indicated with arrows in Fig. 16) are illustrated in Fig. 17 and clearly indicate the disparity in positive buoyancy between the dθdz2 and dθdz3 experiments. (The dθdz2 experiment represents the experiment with the smallest ACBL lapse rate that still yielded DCI.) The time series in Fig. 17 correspond to the time period when the clouds reside within the prescribed lapse rate layer (between

1320 and 2500 m). Both time series exhibit a nearly linear increase in buoyancy within the first ~150 s but while this linear increase in buoyancy persists for the next ~150 s in the dθdz3 experiment, a nearly exponential increase in buoyancy occurs in the dθdz2 experiment. Given that the environment of the dθdz2 experiment is characterized by a larger ACBL lapse rate, it is not surprising to see the buoyancy increase more rapidly in this experiment than in the dθdz3 experiment. However, a rapid increase in buoyancy never materializes in the dθdz3 experiment and, thus, the full release of the thermal instability is being prevented.

Because a convective cloud is not a material surface, the intraexperiment changes and interexperiment differences in buoyancy noted above may not simply be the consequence of processes preventing the full release of thermal instability. Instead, the source of the air into the cloud may differ. Included in Fig. 17 are the mean heights of the source zones for the positively buoyant regions of the convective clouds in each experiment (computed using backward-integrated trajectories). The mean heights are consistently lower in the dθdz3 experiment. A lower source height will mean a higher θ_w source but clearly this is not sufficient to yield larger buoyancy in the dθdz3 experiment. It is also clear that there is no coherent trend in the mean heights for the dθdz3 experiment. If the decrease in buoyancy was the result of a change to a higher average source (lower initial θ_w), then the mean heights should systematically increase as the buoyancy decreases after ~350 s of elapsed time. However, this trend is not apparent. Thus, the observed intraexperiment changes and interexperiment differences in buoyancy are not the result of changes in the source of air.

Because the changes in the source of air into the shallow convective cloud of the dθdz3 experiment are unable to explain the failure of this cloud to evolve into deep convection, DCI failure must be attributable to processes that mitigate the full release of thermal instability. The preceding analysis suggests that DCI failure in experiment dθdz3 is likely a consequence of a deficiency in positive buoyancy and thus that mixing/dilution may be important. The fact that the buoyancy in experiment dθdz3 increases linearly with time along with the apparent steady ascent of the convective cloud (Fig. 17) suggest that, initially, the buoyancy is large enough to support a trend toward deep convection. However, unlike in experiment dθdz2, the rapid increase in buoyancy never appears and the buoyancy slowly decreases as the rate of convective cloud ascent slows. This suggests that mixing/dilution may be truncating the evolution toward deep convection in the dθdz3 experiment.
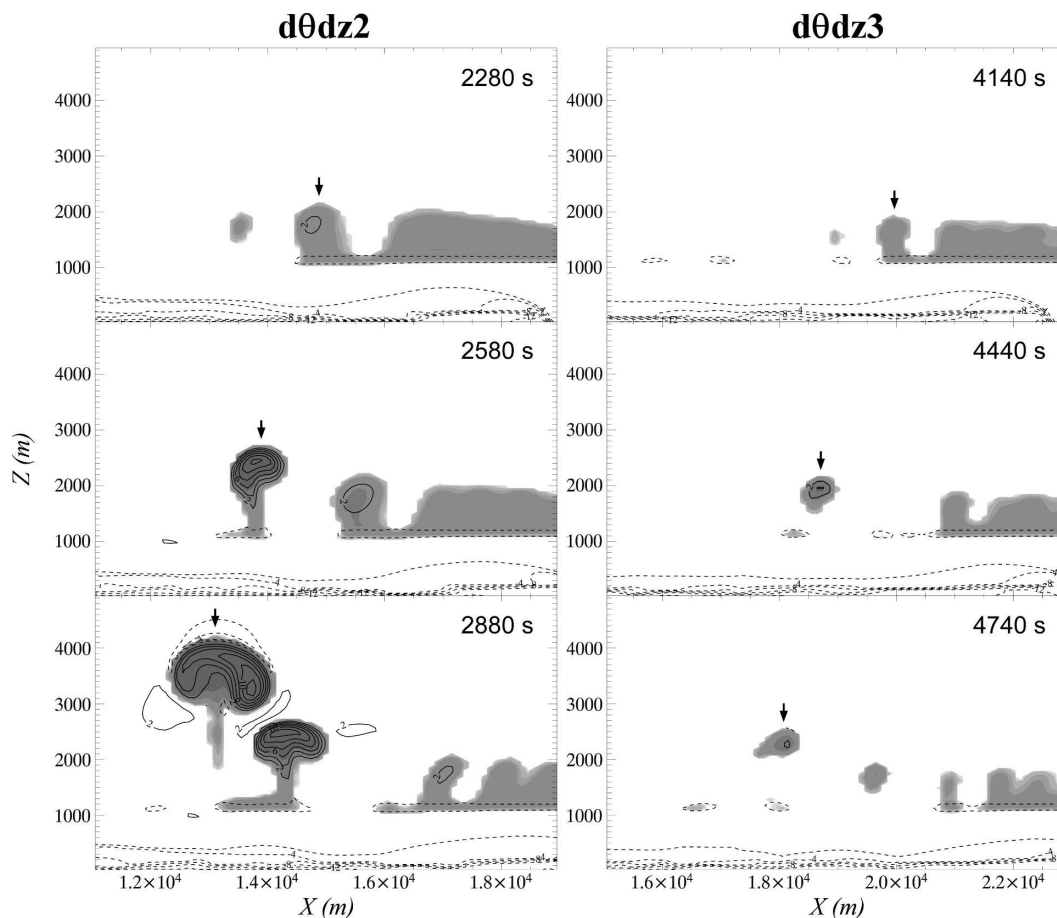
FIG. 16. Evolution of the primary convective clouds in the dθdz2 and dθdz3 experiments. Total cloud (cloud ice plus cloud water) is shaded at a logarithmic interval of 5×10^{-n} kg kg^{-1} from a minimum value of 5×10^{-7} kg kg^{-1}. Buoyancy is contoured every 2×10^{-2} m s^{-2} (negative values appear as broken contours). Arrows denote the primary convective cloud for each experiment.

The best way to quantify the dilution is to consider trajectories through the clouds. Trajectories were backward computed from the regions of the convective clouds with the highest positive buoyancy. Trajectories were then matched based on the source zone and termination altitude (because of the backward integration, this is actually the initial position). Values of θ_w plotted as a function of trajectory height for representative trajectories at three times appear in Fig. 18. The θ_w values are nearly identical early in the evolution of the convective clouds in each experiment (Fig. 18a) with only slightly more dilution in the dθdz3 experiment. However, as the convective clouds continue to evolve, the dilution increases markedly in the dθdz3 experiment, yielding θ_w values that are considerably smaller than those in the dθdz2 experiment (Figs. 18b and 18c). The differences in dilution are in part attributable to the differences in the initial cloud size. As evidenced in Fig. 16, the embryonic convective cloud in dθdz2 at 5880 s

was demonstrably larger (1.7 times larger) than the embryonic convective cloud in dθdz3 at 7740 s. Some of this difference may be a consequence of the larger area of positive buoyancy stemming from the larger ACBL lapse rate in the dθdz2 experiment; however, a more important mechanism appears to be primarily responsible for the increased dilution of the convective cloud of the dθdz3 experiment.

As indicated in Fig. 18, the interexperiment differences in the elapsed times required for the specific trajectories to ascend from 1350 m to the altitude of trajectory initiation (coincidentally 1350 m corresponds to both the approximate bottom of the prescribed lapse rate layer and the level at which the trajectories illustrated in Fig. 18 have the same θ_w) change as the convective cloud evolves. Approximately 200 s after the shallow convective clouds cleave off of the cloud mass at the preexisting boundary, the trajectory of the dθdz3 experiment takes about 15% longer to traverse the
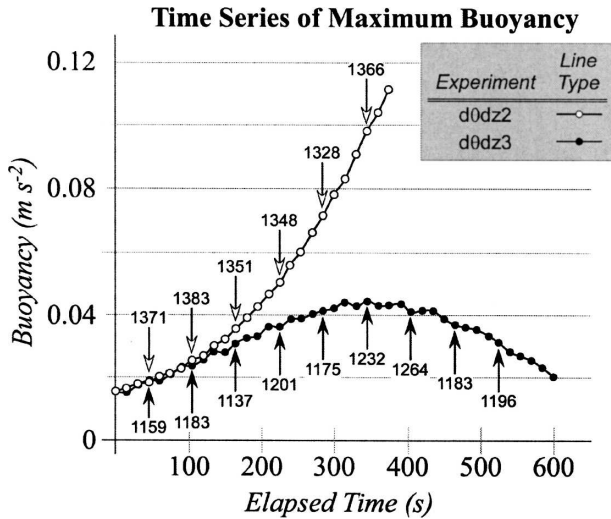
Time Series of Maximum Buoyancy

FIG. 17. Time series of maximum buoyancy within the primary clouds of the dθdz2 and dθdz3 experiments. Elapsed time is measured from 2175 s for dθdz2 and from 4155 s for dθdz3. Numbers atop (below) open (closed) arrows indicate the average source height for air within the positively buoyant cloud for the dθdz2 (dθdz3) experiment at the given time.

same depth as the trajectory of the dθdz2 experiment (Fig. 18a). The same is roughly true of the trajectories at the next times illustrated in Fig. 18b. However, for trajectories that ascend to ~2300 m at 4620 s in dθdz3 and 2580 s in dθdz2 (Fig. 18c) a more prominent inter-experiment disparity in the elapsed times emerges: the trajectories of the dθdz3 experiment take considerably longer to ascend to the same altitude than the trajec-

tories of the dθdz2 experiment. To a large extent, this result should be expected considering that the environment of the dθdz3 experiment has a smaller low-level CAPE density (the portion of the CAPE below a given level) for undiluted parcels originating just above 1000 m (Fig. 19). However, the larger buoyancy force may not be the only factor to consider since a slower trajectory ascent should yield a larger amount of dilution (even if the dilution rates for the trajectories of the two experiments are the same) and the reduction in buoyancy more pronounced. This reduction in buoyancy will lead to a slower ascent (compared to the less diluted result) and will further increase the dilution. Thus, the relationship between dilution and buoyancy/parcel ascent is nonlinear and suggests that two separate convective regimes may exist: a supercritical state capable of supporting DCI and a subcritical state that is unlikely to support DCI. It is important to note that dilution will act to reduce the buoyancy in both subcritical and supercritical conditions. However, in supercritical conditions, the rate of increase in buoyancy due to continued parcel ascent exceeds the reduction in buoyancy due to dilution. Under subcritical conditions, the rate of increase in buoyancy due to parcel ascent is outpaced by the rate of reduction in buoyancy due to dilution and the parcel ascent terminates.

The relationship between the environmental lapse rate and the two convective regimes (one capable of supporting DCI and the other unlikely to support DCI) is illustrated here using a heuristic Lagrangian model. In this model, 1) parcel motion is purely vertical, 2) parcel acceleration is solely dependent on buoyancy, 3)
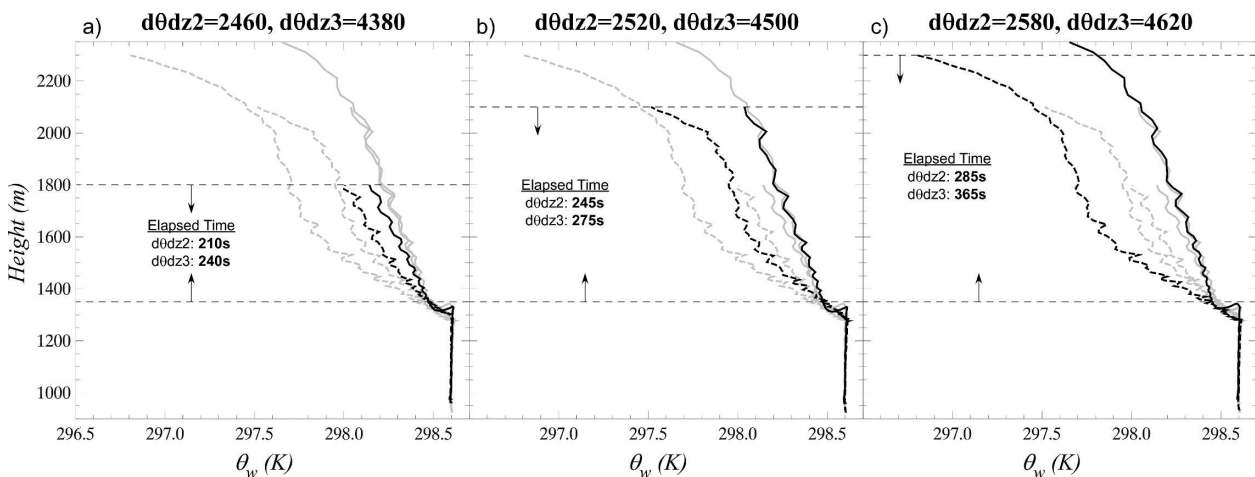

FIG. 18. Values of θ_w plotted as a function of height for representative trajectories from the dθdz2 (continuous curves) and dθdz3 (broken curves) experiments. Trajectories were backward computed for experiment dθdz2 (dθdz3) from (a) 2460 (4380), (b) 2520 (4500), and (c) 2580 s (4620 s). Included in these panels are the elapsed times necessary for the trajectories to ascend from 1350 m to the termination altitude (because of the backward integration, this is actually the initial position). Gray curves are the profiles from the other panels.
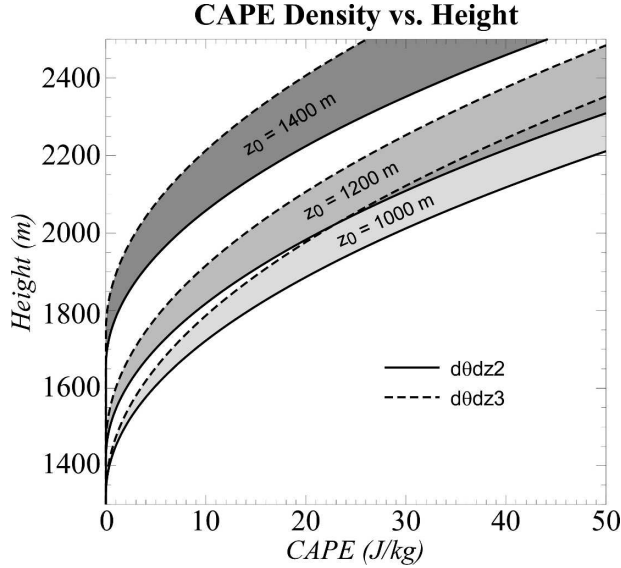
CAPE Density vs. Height

FIG. 19. CAPE density (the portion of the CAPE below a given level) for undiluted parcels plotted as a function of the height below which the CAPE density is computed. The continuous (broken) curves represent profiles for the $d\theta dz2$ ($d\theta dz3$) experiment. CAPE density is computed for three initial parcel heights (z_0): 1000, 1200, and 1400 m. For each z_0 the profiles for each experiment are visually coupled using the shaded envelopes.

θ_w from Heuristic Model

FIG. 20. Values of θ_w plotted as a function of height computed using the heuristic Lagrangian model. Thick curves are associated with the six ACBL lapse rates used in the experiments conducted for this work. Gray curves are for intermediate lapse rates.

the dilution rate (of θ_w) is constant,[3] and 4) in the absence of dilution, θ_w is conserved. The model is solved using the environmental profiles of temperature and moisture used for the experiments conducted for this work. Additional information on the model can be found in appendix B. Results appear in Fig. 20 and clearly illustrate the two regimes. For these conditions, the critical value of Γ is 8.0 K km^{-1} (corresponding to $d\theta_0/dz = 1.985$ K km^{-1}): values of Γ larger than this constitute a supercritical state, would produce parcel ascent through the depth of the domain, and would presumably support DCI. This critical value should not be considered a "magic number" as it is highly sensitive to the choices of dilution rate and initial vertical motion. However, this model clearly illustrates the presence of two regimes for convective clouds that are regulated by the ACBL lapse rate and indicates that the failure of experiment $d\theta dz3$ to yield deep convection is a consequence of the small ACBL lapse rate, which supported subcritical conditions.

---

[3] The validity of such an assumption is uncertain. As the positive buoyancy within a cloud increases, the entrainment should increase, suggesting that the dilution rate should be positively correlated with low-level CAPE density. Including this sensitivity in the heuristic model could shift the critical lapse rate to a smaller value but should not alter the ability of the model to capture the two regimes.
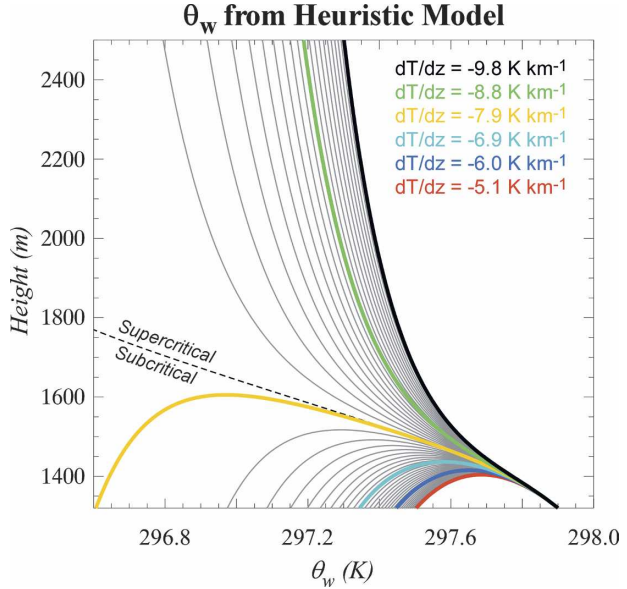
4. Conclusions

The aim of this work was to examine the possible sensitivity of deep convective initiation to the lapse rate of the active cloud-bearing layer. A suite of numerical experiments was conducted using an idealized cloud-scale model. Clouds were initiated using a new technique that involves a preexisting airmass boundary initialized such that the (unrealistic) adjustment of the model state variables to the imposed boundary is disassociated from the simulation of convection. The reference state environments had the same ML-CIN, ML-CAPE, ML-LFC, relative humidity, and wind profiles but varying lapse rates in the ACBL (located between the ML-LFC and 2500 m). The following is a summary of the findings from this work.

- Of the six simulations conducted for the experiment set, only the three environments with the largest ACBL lapse rates supported DCI.
- Among the environments that supported DCI, the time required for initiation decreased with increasing lapse rate and the magnitude of the maximum vertical velocity value for the initial deep convection was positively correlated with the lapse rate.
- Even though density current depths varied little between experiments, the magnitude/depth of the forced ascent increased with the increasing lapse rate of the cloud-bearing layer. This was a consequence of

the smaller values of negative buoyancy within the ACBL for the larger lapse rate environments.

- Despite the presence of a surface-based airmass boundary, deep convection was initiated from elevated sources: parcels in the convective clouds originated near 1300 m and the contribution from air in the well-mixed layer (below 1000 m) was delayed by as much as 1740 s following the first release of thermal instability. Parcels originated near 1300 m because the value of Δz^* was smallest at this level. The quantity Δz^* is the distance a parcel would have to be lifted from its reference height to reach its LFC.

- Thermal instability was more likely to be released in the experiments with larger ACBL lapse rates because the forced ascent at the preexisting boundary was stronger and because the parcels' LFCs were lower, irrespective of parcel dilution.

- A heuristic Lagrangian model was offered that captured the nonlinear relationship between buoyancy and dilution and clearly illustrated the presence of two regimes. In one regime (termed supercritical), the rate of increase in the buoyancy due to parcel ascent exceeds the reduction in the buoyancy due to dilution. DCI is likely in this regime. In the second regime (termed subcritical), the rate of increase in the buoyancy due to parcel ascent is outpaced by the rate of reduction in the buoyancy from dilution. DCI is unlikely in this regime. The transition from subcritical to supercritical conditions is strongly dependent on the environmental lapse rate.

- In experiment dθdz3 parcels did reach their LFCs (thermal instability was released) but deep convection still failed to develop. It was argued that, unlike the experiments with larger ACBL lapse rates, the lapse rate of the dθdz3 experiment yielded subcritical conditions.

This work has shown that the lapse rate of the ACBL will regulate the convective regime irrespective of boundary layer thermodynamics, deep tropospheric vertical shear, and forced ascent and should therefore be considered along with these parameters when attempting to diagnosis and/or predict DCI.
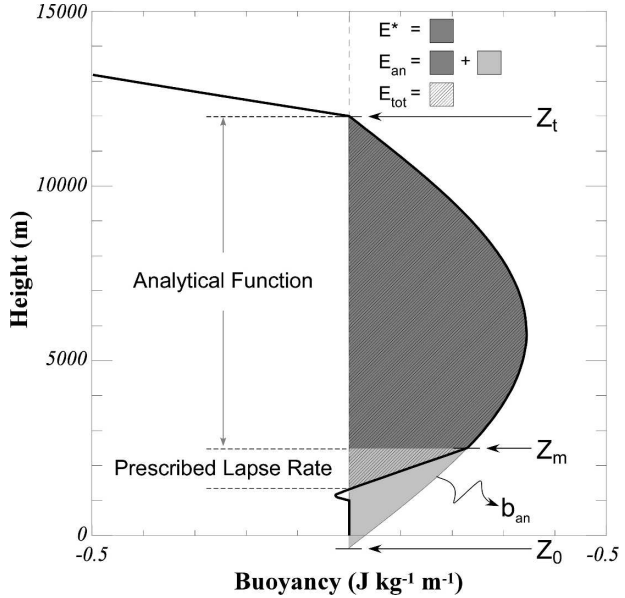
FIG. A1. Illustration of the analytical function used to prescribe the temperature profiles of the experiment soundings. The buoyancy distribution for the sounding appears as a continuous black curve, z_t represents the height of the tropopause, z_0 represents the bottom of the full (untruncated) analytical sounding, z_m represents the top of the prescribed lapse rate layer and bottom of the truncated analytical sounding, the entire shaded region represents the ML-CAPE of the full (untruncated) analytical buoyancy profile (E_{an}), the dark shading represents the ML-CAPE of the truncated analytical buoyancy profile (E^*), and the hatched region represents the ML-CAPE of the final sounding.

APPENDIX A

Analytical Prescription of Reference State Temperature

The reference state temperature profile is prescribed using an analytical function for buoyancy that relates the ML-CAPE within the prescribed lapse rate layer to the fixed-total ML-CAPE. The analytical function is as follows:

$$b_{an} = \frac{\pi}{2(z_t - z_0)} E_{an} \sin\left[\frac{\pi(z - z_0)}{z_t - z_0}\right], \qquad (A1)$$

where b_{an} is the buoyancy (J kg^{-1} m^{-1}). The relationship between the remaining parameters in (A1) is illustrated in Fig. A1 for an example sounding. The parameter z_t is the height of the tropopause, z_0 is the bottom elevation of the full analytical buoyancy distribution, and E_{an} is the ML-CAPE of the full (untruncated) analytical buoyancy profile (equivalent to $\int_{z_0}^{z_t} b_{an} \, dz$).

The magnitude of E_{an}, and therefore the amplitude of the sine profile used in the analytical function, is used to modulate the shape of the buoyancy/temperature

profile above the prescribed lapse rate layer. Because the total ML-CAPE of the final sounding (E_{tot}) is to remain constant between reference state environments, the profile of the buoyancy/temperature *above* the prescribed lapse rate layer must be adjusted to account for the intersounding differences in the ML-CAPE *within* the prescribed lapse rate layer (E_{plr}). For a fixed E_{tot}, the CAPE of the truncated analytical profile, $E*$ (the portion of the analytical profile above the prescribed lapse rate layer; see Fig. A1) must satisfy the following relation:

$$E* = E_{\text{tot}} - E_{\text{plr}}. \tag{A2}$$

With this definition of $E*$, E_{an} can be written as

$$E_{\text{an}} = E* + \int_0^{z_m} b_{\text{an}}\, dz$$

$$= E*\left\langle 1 + \frac{1}{2}\left\{\cos\left[\frac{\pi(z_m - z_0)}{z_t - z_0}\right] - 1\right\}\right\rangle^{-1}, \tag{A3}$$

where z_m is the height of the top of the prescribed lapse rate layer. This equation still contains one unknown, z_0; however, only one value of z_0 will simultaneously satisfy (A3) while ensuring that the *analytical* buoyancy at the top of the prescribed lapse rate layer equals the *prescribed* buoyancy.

APPENDIX B

Heuristic Lagrangian Model

Four key assumptions underpin the heuristic Lagrangian model used for this work. The first assumption is that parcel motion is purely vertical. The second assumption is that parcel acceleration is solely dependent on the buoyancy. In this model, buoyancy accounts for the effect of water vapor on density but excludes precipitation loading. The buoyancy is computed using the diluted θ_w within the parcel and the environmental profiles of temperature and moisture used for the DCI experiments. The third assumption is that the dilution rate is constant. Only the wet-bulb potential temperature is diluted and the dilution rate has been set to 0.002 K s^{-1}. This dilution rate is consistent with the values exhibited by trajectories backward computed from the regions of peak buoyancy within the convective clouds of the dθdz2 and dθdz3 experiments. The fourth key assumption is that θ_w is conserved in the absence of dilution. This model also assumes that the parcel pressure is always identical to the environmental (hydrostatic) pressure.

Parcels are initialized identically, regardless of the environmental profile. It is assumed that the source

TABLE B1. Prescribed parameters in the heuristic Lagrangian model and the specific values used for the experiments conducted.

Parameter	Value
Initial θ_w	297.9 K
Initial height	1320 m
Initial vertical velocity	1.5 m s^{-1}
Dilution rate	0.002 K s^{-1}

height of the parcels is ~1320 m. At this height, the environmental θ_w values are identical between the different environments and have a value of 297.9 K. Parcels are also given an initial upward motion of 1.5 m s^{-1}. A summary of the prescribed parameters appears in Table B1.

REFERENCES

Atkins, N. T., M. L. Weisman, and L. J. Wicker, 1999: The influence of preexisting boundaries on supercell evolution. *Mon. Wea. Rev.,* **127,** 2910–2927.

Bryan, G. H., 2005: Spurious convective organization in simulated squall lines owing to moist absolutely unstable layers. *Mon. Wea. Rev.,* **133,** 1978–1997.

——, and J. M. Fritch, 2002: A benchmark simulation for moist nonhydrostatic numerical models. *Mon. Wea. Rev.,* **130,** 2917–2928.

Coniglio, M. C., D. J. Stensrud, and L. J. Wicker, 2006: Effects of upper-level shear on the structure and maintenance of strong quasi-linear mesoscale convective systems. *J. Atmos. Sci.,* **63,** 1231–1252.

Dudhia, J., and M. W. Moncrieff, 1989: A three-dimensional numerical study of an Oklahoma squall line containing right-flank supercells. *J. Atmos. Sci.,* **46,** 3363–3391.

Fovell, R. G., 2005: Convective initiation ahead of the sea-breeze front. *Mon. Wea. Rev.,* **133,** 264–278.

——, and P. S. Dailey, 1995: The temporal behavior of numerically simulated multicell-type storms. Part I: Modes of behavior. *J. Atmos. Sci.,* **52,** 2073–2095.

——, and P.-H. Tan, 1998: The temporal behavior of numerically simulated multicell-type storms. Part II: The convective cell life cycle and cell regeneration. *Mon. Wea. Rev.,* **126,** 551–577.

——, and ——, 2000: A simplified squall-line model revisited. *Quart. J. Roy. Meteor. Soc.,* **126,** 173–188.

Garner, S. T., and A. J. Thorpe, 1992: The development of organized convection in a simplified squall-line model. *Quart. J. Roy. Meteor. Soc.,* **118,** 101–124.

Gilmore, M. S., and L. J. Wicker, 1998: The influence of midtropospheric dryness on supercell morphology and evolution. *Mon. Wea. Rev.,* **126,** 943–958.

——, J. M. Straka, and E. N. Rasmussen, 2004a: Precipitation evolution sensitivity in simulated deep convective storms: Comparisons between liquid-only and simple ice and liquid phase microphysics. *Mon. Wea. Rev.,* **132,** 1897–1916.

——, ——, and ——, 2004b: Precipitation uncertainty due to variations in precipitation particle parameters within a simple microphysics scheme. *Mon. Wea. Rev.,* **132,** 2610–2627.

Hane, C. E., 1975: The trajectories of dropsondes in simulated thunderstorm circulations. *Mon. Wea. Rev.,* **103,** 709–716.

Houston, A. L., 2004: The role of preexisting airmass boundaries in the maintenance and rotation of deep convection in a high-CAPE, low-shear environment. Ph.D. thesis, Dept. of Atmospheric Sciences, University of Illinois at Urbana–Champaign, 275 pp.

Johnson, R. H., and B. E. Mapes, 2001: Mesoscale processes and severe convective weather. *Severe Convective Storms, Meteor. Monogr.,* No. 50, Amer. Meteor. Soc., 71–122.

Klemp, J. B., and R. B. Wilhelmson, 1978: The simulation of three-dimensional convective storm dynamics. *J. Atmos. Sci.,* **35,** 1070–1096.

Lee, B. D., and R. B. Wilhelmson, 1997: The numerical simulation of nonsupercell tornadogenesis. Part II: Evolution of a family of tornadoes along a weak outflow boundary. *J. Atmos. Sci.,* **54,** 2387–2415.

Lin, Y.-L., R. L. Deal, and M. S. Kulie, 1998: Mechanisms of cell regeneration, development, and propagation within a two-dimensional multicell storm. *J. Atmos. Sci.,* **55,** 1867–1886.

Liu, C., and M. W. Moncrieff, 1996: A numerical study of the effects of ambient flow and shear on density currents. *Mon. Wea. Rev.,* **124,** 2282–2303.

——, and ——, 2000: Simulated density currents in idealized stratified environments. *Mon. Wea. Rev.,* **128,** 1420–1437.

Murray, F. W., 1970: Numerical models of a tropical cumulus cloud with bilateral and axial symmetry. *Mon. Wea. Rev.,* **98,** 14–28.

Ogura, Y., 1963: The evolution of a moist convective element in a shallow, conditionally unstable atmosphere: A numerical calculation. *J. Atmos. Sci.,* **20,** 407–424.

Peckham, S. E., and L. J. Wicker, 2000: The influence of topography and lower-tropospheric winds on dryline morphology. *Mon. Wea. Rev.,* **128,** 2165–2189.

——, R. B. Wilhelmson, L. J. Wicker, and C. L. Ziegler, 2004: Numerical simulation of the interaction between the dryline and horizontal convective rolls. *Mon. Wea. Rev.,* **132,** 1792–1812.

Purdom, J. F. W., 1982: Subjective interpretations of geostationary satellite data for nowcasting. *Nowcasting,* K. Browning, Ed., Academic Press, 149–166.

Rotunno, R., J. B. Klemp, and M. L. Weisman, 1988: A theory for strong, long-lived squall lines. *J. Atmos. Sci.,* **45,** 463–485.

Schlesinger, R. E., 1984: Effects of the pressure perturbation field in numerical models of unidirectionally sheared thunderstorm convection: Two versus three dimensions. *J. Atmos. Sci.,* **41,** 1571–1587.

Stull, R. B., 1985: A fair-weather cumulus cloud classification scheme for mixed-layer studies. *J. Climate Appl. Meteor.,* **24,** 49–56.

Weckwerth, T. M., and D. B. Parsons, 2006: A review of convection initiation and motivation for IHOP_2002. *Mon. Wea. Rev.,* **134,** 5–22.

Weisman, M. L., and R. Rotunno, 2004: "A theory for strong long-lived squall lines" revisited. *J. Atmos. Sci.,* **61,** 361–382.

Wicker, L. J., and R. B. Wilhelmson, 1995: Simulation and analysis of tornado development and decay within a three-dimensional supercell thunderstorm. *J. Atmos. Sci.,* **52,** 2675–2703.

——, and W. C. Skamarock, 1998: A time-splitting scheme for the elastic equations incorporating second-order Runge–Kutta time differencing. *Mon. Wea. Rev.,* **126,** 1992–1999.

——, M. P. Kay, and M. P. Foster, 1997: STORMTIPE-95: Results from a convective storm forecast experiment. *Wea. Forecasting,* **12,** 388–398.

Wilson, J. W., and W. E. Schreiber, 1986: Initiation of convective storms at radar-observed boundary-layer convergence lines. *Mon. Wea. Rev.,* **114,** 2516–2536.

——, and R. D. Roberts, 2006: Summary of convective storm initiation and evolution during IHOP: Observational and modeling perspective. *Mon. Wea. Rev.,* **134,** 23–47.

Xu, Q., 1992: Density currents in shear flows—A two-fluid model. *J. Atmos. Sci.,* **49,** 511–524.

——, M. Xue, and K. K. Droegemeier, 1996: Numerical simulations of density currents in sheared environments within a vertically confined channel. *J. Atmos. Sci.,* **53,** 770–786.

Xue, M., 2002: Density currents in shear flows: Effects of rigid lid and cold-pool internal circulation, and application to squall line dynamics. *Quart. J. Roy. Meteor. Soc.,* **128,** 47–74.

——, Q. Xu, and K. K. Droegemeier, 1997: A theoretical and numerical study of density currents in nonconstant shear flows. *J. Atmos. Sci.,* **54,** 1998–2019.

Ziegler, C. L., and E. N. Rasmussen, 1998: The initiation of moist convection at the dryline: Forecasting issues from a case study perspective. *Wea. Forecasting,* **13,** 1106–1131.

——, T. J. Lee, and R. A. Pielke Sr., 1997: Convective initiation at the dryline: A modeling study. *Mon. Wea. Rev.,* **125,** 1001–1026.